

OPEN ACCESS

Performance Investigations on All-Solid-State Polymer-Ceramic Sodium-Ion Batteries through a Spatially Resolved Electrochemical Model

To cite this article: F. Gerbig *et al* 2024 *J. Electrochem. Soc.* **171** 090515

View the [article online](#) for updates and enhancements.

You may also like

- [Improving the performance of computer-aided detection of subtle breast masses using an adaptive cueing method](#)
Xingwei Wang, Lihua Li, Weidong Xu et al.
- [A review of computational optimization of bone scaffold architecture: methods, challenges, and perspectives](#)
Ali H Foroughi, Caleb Valeri and Mir Jalil Razavi
- [Two-stage re-parameterization and sample disentanglement network for surveillance vehicle detection](#)
Wei Xie, Weiming Liu and Yuan Dai

ECC-Opto-10 Optical Battery Test Cell: Visualize the Processes Inside Your Battery!

EL-CELL[®]
electrochemical test equipment

- ✓ **Battery Test Cell for Optical Characterization**
Designed for light microscopy, Raman spectroscopy and XRD.
- ✓ **Optimized, Low Profile Cell Design (Device Height 21.5 mm)**
Low cell height for high compatibility, fits on standard samples stages.
- ✓ **High Cycling Stability and Easy Handling**
Dedicated sample holders for different electrode arrangements included!
- ✓ **Cell Lids with Different Openings and Window Materials Available**



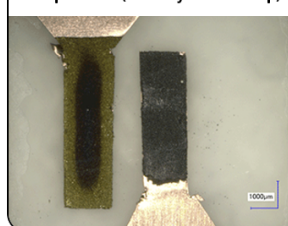
Contact us:

☎ +49 40 79012-734

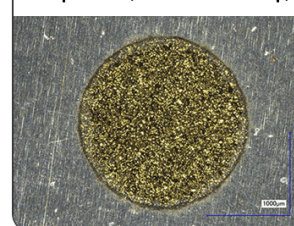
✉ sales@el-cell.com

🌐 www.el-cell.com

Sample Test (Side-by-Side Setup)



Sample Test (Face-to-Face Setup)





Performance Investigations on All-Solid-State Polymer-Ceramic Sodium-Ion Batteries through a Spatially Resolved Electrochemical Model

F. Gerbig,[✉] A. Chauhan,[✉] S. Gietl, and H. Nirschl

Institute of Mechanical Process Engineering and Mechanics, Karlsruhe Institute of Technology (KIT), 76131 Karlsruhe, Germany

Rechargeable batteries are crucial in modern energy storage, with lithium-ion batteries dominating the market. However, the scarcity and environmental concerns associated with lithium have spurred interest in alternative battery chemistries, particularly sodium-ion batteries (SIBs), which utilize abundant sodium resources. Despite extensive experimental research on all-solid-state SIBs (ASSSIBs), theoretical investigations have primarily focused on molecular-level analyses, overlooking the impact of cell composition on overall performance. This paper aims to address this gap by developing a physical model for simulating ASSSIBs at the particle scale. Our methodology involves integrating experimental data with simulation results to identify key factors influencing battery performance. The study reveals slow sodium ion transport as a significant bottleneck, attributed to factors such as low porosity of the half-cell and limited electrolyte ionic conductivity. Simulation outcomes emphasize the importance of advancing fast-ion-conducting solid electrolytes to enhance ASSSIB performance. Moreover, the results suggest that electrodes with high electrolyte active filler content and reduced thickness are necessary for achieving optimal battery capacity utilization. Overall, this research underscores the intricate relationship between electrode microstructure and battery performance, offering valuable insights for the design and optimization of sustainable sodium-ion battery systems suitable for stationary and mobile applications.

© 2024 The Author(s). Published on behalf of The Electrochemical Society by IOP Publishing Limited. This is an open access article distributed under the terms of the Creative Commons Attribution 4.0 License (CC BY, <http://creativecommons.org/licenses/by/4.0/>), which permits unrestricted reuse of the work in any medium, provided the original work is properly cited. [DOI: 10.1149/1945-7111/ad7763]



Manuscript submitted June 12, 2024; revised manuscript received July 26, 2024. Published September 13, 2024.

List of Symbols

c_{el}	electrolyte sodium ion concentration, mol m^{-3}
c_s	active material sodium concentration, mol m^{-3}
D_{el}	electrolyte sodium ion diffusion coefficient, $\text{m}^2 \text{s}^{-1}$
D_s	active material sodium diffusion coefficient, $\text{m}^2 \text{s}^{-1}$
F	Faraday constant, C mol^{-1}
i_{BV}	Butler–Volmer current density, A m^{-2}
i_0	exchange current density, A m^{-2}
i_{el}	electrolyte current density, A m^{-2}
i_s	active material current density, A m^{-2}
k	Butler–Volmer reaction constant, $\text{m}^{2.5} \text{mol}^{-0.5} \text{s}^{-1}$
K_{NaTFSI}	ionic conductivity prefactor for the PEO–NaTFSI system, M^{-1}
\mathbf{n}	surface unit normal vector pointing outside the computational domain
R	universal gas constant, $\text{J mol}^{-1} \text{K}^{-1}$
s_i	signed stoichiometric coefficient
t_+^0	transference number of sodium ions in the electrolyte
T	temperature, K
U_{eq}	equilibrium potential, V
q	physical quantity
$\varphi_{\text{el,fil}}$	electrolyte active filler volume fraction
$\varphi_{\text{el,pol}}$	electrolyte polymer volume fraction
κ	electrolyte ionic conductivity, S m^{-1}
κ_{d}	electrolyte diffusional conductivity, S m^{-1}
ν	number of moles of ions into which a mole of electrolyte dissociates
ν_i	moles of ion i produced when a mole of its salt dissociates
Φ_{el}	electrolyte potential, V
Φ_s	active material potential, V
σ	active material conductivity, S m^{-1}
χ	mole fraction, M M^{-1}

Rechargeable batteries have become integral to modern society due to their scalability, cost-efficiency, and high energy storage capabilities.¹ Lithium-ion batteries (LIBs) have emerged as frontrunners, experiencing widespread commercial success in portable electronics and electric vehicles owing to their impressive energy density and extended lifespan. Research on sodium-ion batteries (SIBs or SIBs) commenced concurrently with lithium-ion batteries (LIBs) in the late 1970s but saw limited success, leading to a hiatus in research for several decades. However, interest in SIBs revived in the late 2000s, making it a vibrant area of study today. The main drive behind this resurgence is the desire to develop batteries using abundant and non-critical elements.² Sodium is much more abundant than lithium and is distributed evenly across the globe, making it a sustainable alternative to lithium, which is considered a critical element by the EU.³ Particularly, the increasing need for energy storage applications with lower energy density requirements, such as stationary battery storage, necessitates the development of new battery chemistries. The rising demand for LIBs has caused lithium prices to soar due to its scarcity, thereby undermining its feasibility for large-scale energy storage solutions. Nonetheless, for batteries to be genuinely sustainable, it is essential not only to substitute lithium with sodium but also to remove other critical metals such as cobalt. The chemical composition of sodium cathode materials presents numerous opportunities to utilize alternative and abundant elements like iron, manganese, and copper, thereby decreasing dependence on critical materials like cobalt and nickel found in LIBs.⁴ Moreover, the manufacturing processes for SIBs are similar to those for LIBs, which lowers the barriers to large-scale production. Nevertheless, the larger size and weight of sodium ions compared to lithium ions result in challenges such as poor phase stability, sluggish ion transport kinetics, and undesirable interphase formation in sodium host materials.

Cathode materials, as vital constituents of SIBs, play a pivotal role in providing active sodium ions, determining operational voltage, and significantly contributing to overall battery cost (up to 32%).⁵ In comparison to traditional stationary battery technologies such as lead-acid batteries, SIBs provide a notable enhancement in energy density. This makes them ideal for stationary energy storage

[✉]E-mail: felix.gerbig@kit.edu

applications and small vehicles where high-end Li-ion batteries are not required. From a scientific perspective, substituting lithium with sodium in electrochemical cells raises intriguing questions due to the larger size of sodium ions, affecting various properties like diffusion, phase behavior, and charge transfer. Research on SIBs primarily focused on developing active materials similar to those in Li-ion batteries (LIBs), but performance remains subpar.

The electrolyte, which is frequently overlooked, holds significant importance in sodium-ion batteries, as it facilitates the transportation of Na^+ ions between the cathode and the anode. Furthermore, its decomposition products contribute to the formation of the solid-electrolyte interphase (SEI) and the cathode-electrolyte interphase (CEI), which play a crucial role in various aspects of SIB performance, including cycle life, rate capability, and safety.⁶ Most intercalation chemistry based battery systems utilize organic solvents, which offer significant advantages due to their high room-temperature ionic conductivity and their ability to accommodate reversible volume expansion of electrode particles during cycling.⁷ On the other hand, their limited electrochemical and thermal stability imposes strict safety constraints on liquid electrolyte cells, thereby affecting the maximum achievable energy and power density of such cells. An additional concern is that, metallic sodium irreversibly reacts with organic electrolytes which leads to SEI formation thus promoting dendrite growth.⁸ The use of sodium metal anodes with a high theoretical specific capacity of 1166 mAh g^{-1} promises a significant boost in the theoretical capacity of sodium-ion batteries. To date, researchers have struggled to make use of purely sodium metal anodes through uncontrolled dendrite growth.

Addressing these challenges inherent in liquid electrolytes is the central goal of solid-state batteries (SSBs). These batteries feature a solid electrolyte, in contrast to the liquid electrolytes used in conventional batteries. The category of solid electrolytes encompasses a wide range of materials, including organic polymers, inorganic crystals, glassy phases, or hybrid compositions. Each subtype of solid electrolyte has unique properties, conduction mechanisms, and degradation mechanisms.^{9–11} There is a critical need for alternative materials offering improved attributes such as rate capability and cost-effectiveness.

Polymers, often overlooked, play vital roles in battery components, aiding in adhesion, ionic conduction, and material stability. As we transition from LIBs to SIBs, polymers offer versatility for customized chemistries with advanced properties and sustainable production methods. Research on polymer electrolytes has particularly focused on polyethylene oxide (PEO). This polymer stands out for its relatively high levels of ionic conductivity and transference number. Typically, polymer electrolytes are combined with sodium salts to augment conductivity, with NaTFSI standing out as a particularly effective salt due to the plasticizing influence of the TFSI ion. Unfortunately, solid polymer electrolytes still suffer insufficient ionic conductivity at ambient temperatures.

In contrast, inorganic solid electrolytes exhibit high ionic conductivity, yet they are rigid and brittle, which results in elevated contact resistance and complicates the manufacturing process of the cells. A hybrid polymer-ceramic electrolyte overcomes the need to operate at high temperatures by combining the advantages of fast ion-conducting inorganic ceramic particles and mechanically flexible polymers.¹² In recent years, a category of ceramic fillers that actively engage in facilitating sodium ion transport has emerged.¹³ These fillers are consequently referred to as active fillers. NaSICON-type materials, which stands for *Sodium Super Ionic Conductor*, are a type of active fillers and demonstrate both high conductivity and chemical stability. Their synthesis does not necessarily involve critical elements, which makes them ideal active fillers for sustainable sodium-ion batteries.¹⁴ The proposed cell design features a non-porous NaSICON-type separator. Its robust nature and chemical stability are compatible with sodium-metal anode.

While there is a growing body of literature experimentally investigating materials and designs for all-solid-state sodium-ion batteries (ASSSIBs), theoretical approaches have mainly focused on exploring active materials and electrolytes on the molecular level.^{15,16}

However, simulation studies on SIBs have predominantly concentrated on traditional systems featuring liquid electrolytes. For instance, Xiang et al. used equivalent circuit models for state-of-charge and state-of-health estimations.¹⁷ Similarly, Chayambuka et al. proposed the application of pseudo-two-dimensional models (P2D) for SIBs, utilizing fluorinated sodium vanadium phosphate in the positive electrode and hard carbon in the negative electrode.¹⁸ Building on these findings, Garipati et al. developed a reduced-order single-particle-model that achieves quick computation times and low computational cost while preserving the accuracy of the P2D model.¹⁹

The current shift from liquid electrolytes to solid or hybrid systems opens up a new field of research, presenting unique challenges and opportunities for simulation studies.²⁰ Solid-state electrolytes, with their potential for improved safety and stability, require different modeling approaches to accurately capture their behavior and interactions within the battery system. This necessitates the development of advanced simulation techniques that can account for the complex phenomena occurring at the interfaces and within the bulk of solid-state materials.

To address these emerging challenges, our work aims to explore the effects of cell composition on the overall battery performance at the particle level for the first time. We employ a physics-based microstructure model that resolves the particle scale, allowing us to investigate the impact of various material properties and design parameters on the electrochemical performance of ASSSIBs. By simulating the intricate interactions and transport processes within the battery, this approach provides deeper insights into the factors influencing battery efficiency and longevity, thereby guiding the development of more effective and reliable ASSSIBs. Figure 1 illustrates the working principle of an all-solid-state sodium-ion battery, featuring NaSICON active fillers embedded in a PEO matrix as the electrolyte. Physics-based models offer the advantage of being able to extrapolate data—predicting performance in scenarios that lie outside the boundaries of the original data used to generate the model—with sufficient parameterization and without large sets of experimental data. Such continuum models have been effectively used to study particle properties in LIBs and thereby predicting their effects on the cell performance and enhancing the understanding of otherwise inaccessible processes within the battery cell.^{21,22}

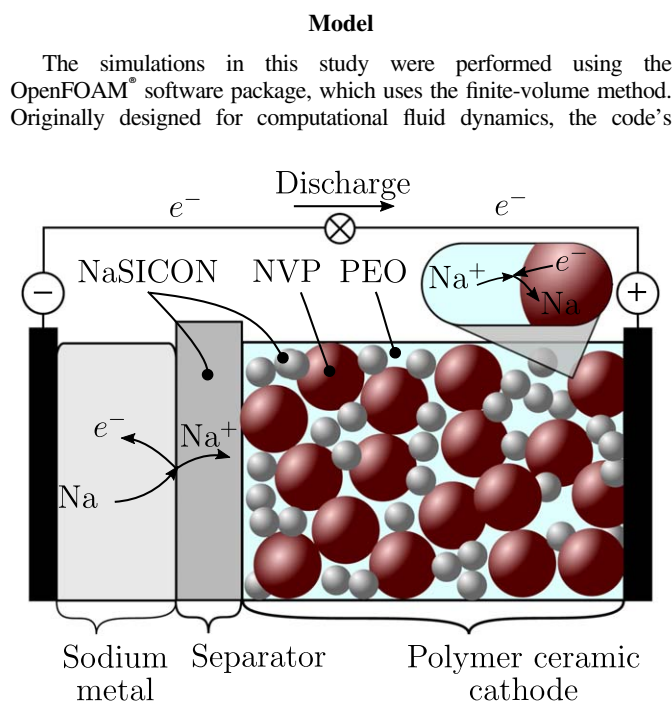
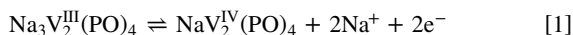


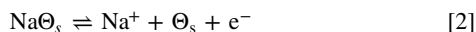
Figure 1. Working principle of an all-solid-state sodium-ion battery with a sodium metal anode and a hybrid polymer-ceramic electrolyte.

versatility and open-source nature allowed us to customize it to accommodate the implementation of governing equations and boundary conditions required for the electrochemical model underlying our research. The numerical solver employed in this study is derived from a preexisting solver developed for lithium-ion batteries, suitably adapted to model sodium-ion batteries with hybrid electrolytes.²³ The model presented uses concentrated solution theory to describe the potential and species distribution in a binary electrolyte.²⁴ The implementation of the model can accommodate various active materials and electrolytes by suitably modifying the physical parameters.

Governing equations.—Polyanion-type sodium vanadium phosphate (NVP) stands out as one of the most extensively researched active materials for SIBs exhibiting remarkable stability, promising capacity and excellent cyclability.²⁵ In this study, NVP serves as the active cathode material with the net reaction of the sodium-ion battery:



It involves the following reaction at the insertion electrode, where Θ_s represents a site in the active material, with a potential of approximately 3.4 V vs Na^+/Na with oxidation of $\text{V}^{3+/4+}$.



The mathematical model relies on five coupled equations describing mass and charge conservation in the solid insertion electrode and the electrolyte. In the active material, electrons transport charge, governed by Ohm's law, which defines the current density within a homogeneous, crystalline solid:

$$i_s = -\sigma \nabla \Phi_s \quad [3]$$

where σ is the active material conductivity and Φ_s the active material potential. The NVP itself exhibits an electric conductivity as low as $3 \times 10^{-8} \text{ S cm}^{-1}$.²⁶ The model incorporates the conductivity-enhancing effect of carbon coating in a constant electric conductivity. Assuming that electrons move faster than other processes, the charge density remains constant $\frac{\partial \rho_v}{\partial t} = 0$ thus resulting in the following equation of continuity for the solid potential:

$$\nabla \cdot i_s = 0 \quad [4]$$

In accordance with Fick's first law, the molar flux density of sodium is proportional to the concentration gradient. The continuity equation depending on the active material sodium diffusion coefficient (D_s) is then represented by Fick's second law:

$$\frac{\partial c_s}{\partial t} = \nabla \cdot D_s \nabla c_s \quad [5]$$

The Na^+ transport in the electrolyte is modeled by concentrated solution theory which is believed to be more precise than simple dilute solution theory. The sodium flux in a binary electrolyte considering diffusion and migration and depending on the electrolyte sodium ion diffusion coefficient (D_{el}), the transference number of sodium ions in the electrolyte (t_+^0), the electrolyte sodium ion concentration (c_{el}), the Faraday constant (F) and the electrolyte current density (i_{el}) is expressed as:

$$J_{c_{\text{el}}} = -D_{\text{el}} \left(1 - \frac{d \ln c_{\text{el},0}}{d \ln c_{\text{el}}} \right) \nabla c_{\text{el}} + \frac{i_{\text{el}} t_+^0}{F} \quad [6]$$

The convection contribution is disregarded in this analysis due to the fact that the solvent velocity in solid electrolytes is typically zero. A comprehensive derivation of the equation from the Maxwell-Stefan

relationship can be found in Ref. 27. In this study the thermodynamic factor $1 - \frac{d \ln c_{\text{el},0}}{d \ln c_{\text{el}}}$ is set to 1. From this, the mass-balance equation for the electrolyte is derived:

$$\frac{\partial c_{\text{el}}}{\partial t} = \nabla \cdot D_{\text{el}} \nabla c_{\text{el}} - \frac{\nabla \cdot (i_{\text{el}} t_+^0)}{F} \quad [7]$$

We enforce charge conservation in the electrolyte which states that $\nabla \cdot i_{\text{el}} = 0$. The electric current density field is divergence-free, as the macroscopic model does not resolve double layer formation $\frac{\partial \Phi_{\text{el}}}{\partial t} = 0$. In a binary electrolyte, the electrolyte current density is

$$i_{\text{el}} = -\kappa \nabla \Phi_{\text{el}} - \frac{\nu \kappa R T}{F} \left(\frac{s_+}{n \nu_+} \frac{t_+^0}{z_+ \nu_+} \frac{s_0 c_{\text{el}}}{n c_0} \right) \nabla \ln c_{\text{el}} \quad [8]$$

with signed stoichiometric coefficient (s_i), moles of ion i produced when a mole of its salt dissociates (ν_i), number of moles of ions into which a mole of electrolyte dissociates (ν) and the number of electrons produced by the reaction (n).²⁸ Unlike Eqs. 3, 8 includes an additional diffusion term on the right-hand side, representing ion movement in an electrolyte due to a concentration gradient.²⁷ The concentration dependence of the electrolyte ionic conductivity (κ) of a polymer is described by a semi-empirical equation inspired by the work of Mongcopa et al.:²⁹

$$\kappa(c_{\text{el}}) = \kappa_{\text{NaTFSI}}(T) c_{\text{el}} \left[\exp \left(- \frac{c_{\text{el}}}{c_{\text{el}, \kappa_{\text{max}}}(T)} \right) \right] \quad [9]$$

No negatively charged species participate in the reaction ($s_- = 0$), NaTFSI fully dissociates in PEO and the solvent does not participate in the reaction ($s_0 = 0$), the coefficient of Na^+ is -1 ($s_+ = -1$), one electron is produced in the reaction ($n = 1$). Also, $\nu_+ = \nu_- = z_+ = 1$ for most salts and with the introduction of the electrolyte diffusional conductivity (κ_d)

$$\kappa_d = \frac{2RT\kappa}{F} (1 - t_+^0) \quad [10]$$

Equation 8 simplifies to

$$i_{\text{el}} = -\kappa \nabla \Phi_{\text{el}} + \frac{\kappa_d}{c_{\text{el}}} \nabla c_{\text{el}} \quad [11]$$

A fifth equation to couple the four partial differential equations (PDEs) described in Eqs. 4, 5, 7, and the continuity equation of the electrolyte ($\nabla \cdot i_{\text{el}} = 0$) is needed. It computes the rate at which sodium is produced or consumed by the electrochemical surface reaction. This equation accounts for the vital charge transfer kinetics at the active material surface and in the electrolyte, which adhere to the widely recognized Butler–Volmer equation:^{24,30}

$$i_{\text{BV}} = i_0 \left[\exp \left(\frac{\alpha_a F}{RT} (\Phi_s - \Phi_{\text{el}} - U_{\text{eq}}(c_s)) \right) - \exp \left(- \frac{\alpha_c F}{RT} (\Phi_s - \Phi_{\text{el}} - U_{\text{eq}}(c_s)) \right) \right] \quad [12]$$

It is a modeling approach to express the net charge transfer rate resulting from the heterogeneous reaction occurring on the electrolyte–cathode surface. The Butler–Volmer current density depends on exchange current density (i_0) along with the local overpotential. In the absence of more detailed information about reaction mechanisms, the charge transfer reaction is typically assumed symmetric, therefore setting the anodic and cathodic transfer coefficients α_a, α_c to 0.5 yielding:²⁸

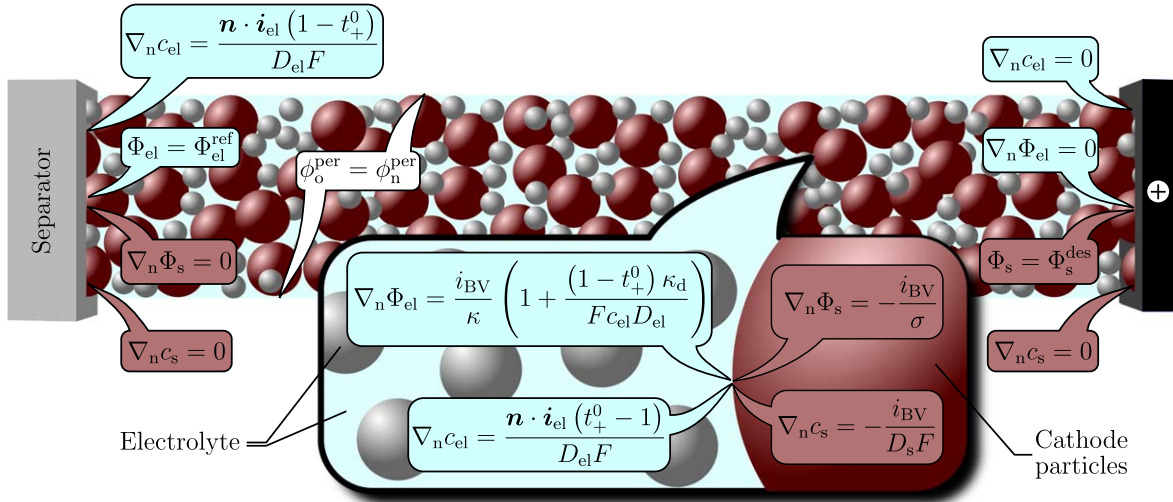


Figure 2. Illustration of the boundary and interface conditions employed in the computational model of the cathode half-cell of an all-solid-state sodium-ion battery. The surface normal gradient is denoted by $\nabla_n \phi$, which represents the dot product $\mathbf{n} \cdot \nabla \phi$.

$$i_0 = Fk \sqrt{c_{s,\max} - c_s} \sqrt{c_s} \sqrt{c_{el}} \quad [13]$$

i_0 describes the dynamic equilibrium of the charge transfer reaction and quantifies the amount of electrons exchanged back and forth when the electrode is at rest. Typically, experimental measurements are necessary to determine the ButlerVolmer reaction constant (k) and the equilibrium potential (U_{eq}).

Boundary conditions.—Selecting appropriate boundary conditions is crucial for solving the model. The Neumann-style boundary condition for the active material potential at the cathode-to-electrolyte (cte) interface using the surface unit normal vector pointing outside the computational domain (n) is given by:

$$\mathbf{n} \cdot \nabla \Phi_s|_{cte} = -\frac{i_{BV}}{\sigma} \quad [14]$$

Figure 2 provides an overview of the boundary and interface conditions implemented in the presented model. For clarity, our illustrations adopt the notation $\nabla_n \phi$ to denote the gradient of a scalar quantity ϕ in the direction of the surface normal vector \mathbf{n} . This is equivalent to the dot product $\nabla \phi \cdot \mathbf{n}$. The active material sodium concentration boundary gradient at the cte is calculated accordingly, while the gradient at the separator equals zero:

$$\mathbf{n} \cdot \nabla c_s|_{sep} = 0, \quad \mathbf{n} \cdot \nabla c_s|_{cte} = -\frac{i_{BV}}{D_s F} \quad [15]$$

The flux of the anion into the separator and the active material is zero. Instead, its diffusion is balanced by migration, which establishes the boundary conditions for electrolyte sodium ion concentration:

$$\begin{aligned} \mathbf{n} \cdot \nabla c_{el}|_{sep} &= -\frac{\mathbf{n} \cdot \mathbf{i}_{el}(1 - t_+^0)}{D_{el} F}, \\ \mathbf{n} \cdot \nabla c_{el}|_{etc} &= \frac{i_{BV}(1 - t_+^0)}{D_{el} F} \end{aligned} \quad [16]$$

Substituting 16 in the flux-density equation leads to the expression for the electrolyte potential:

$$\mathbf{n} \cdot \nabla \Phi_{el}|_{etc} = \frac{i_{BV}}{\kappa} \left(1 + \frac{(1 - t_+^0) \kappa_d}{F c_{el} D_{el}} \right) \quad [17]$$

The periodic setup introduces additional boundaries, necessitating the implementation of specific boundary conditions. These boundary conditions ensure that the flux densities exiting one side of the domain and entering the other side are equal, and that the potential and concentration values remain consistent across both sides. The standard Neumann or Dirichlet boundary conditions are inadequate for fulfill the requisite specifications, necessitating the utilization of Robin-type boundary conditions. In OpenFOAM, a scalar value at the boundary for such a boundary condition is determined using the equation:

$$\phi_f = w \phi_{ref} + (1 - w)(\phi_c + \Delta \nabla \phi_{ref}) \quad [18]$$

The value located at the center of the boundary cell is represented by (ϕ_c). The necessary reference values (ϕ_{ref}), reference gradients ($\nabla \phi_{ref}$) and value fractions (w) are obtained by ensuring charge conservation ($\mathbf{i}_o = \mathbf{i}_n$) and mass conservation ($\mathbf{J}_o = \mathbf{J}_n$) between the periodic patches and compare coefficients with the equation above (see Table I). In this context, the subscript n denotes the neighboring

Table I. Boundary conditions for the periodic setup in the OpenFOAM® simulation environment, ensuring consistent flux densities, potentials, and concentrations across the periodic boundaries of the computational domain.

Quantity	Reference value (ϕ_{ref})	Reference gradient ($\nabla \phi_{ref}$)	Value fraction (w)
Φ_{el}	$\Phi_{el,n}$	$\frac{2RT}{F c_{el,o}} (t_+^0 - 1) \nabla c_{el,o} - \frac{\kappa_{d,n}}{c_{el,n} \kappa} \nabla c_{el,n}$	$\frac{\kappa_n \Delta n}{\kappa_n \Delta n + \kappa_o \Delta n}$
c_{el}	$c_{el,n}$	0	$\frac{D_{el,n} \Delta n}{D_{el,n} \Delta n + D_{el,o} \Delta n}$
Φ_s	$\Phi_{s,n}$	0	0.5
c_s	$c_{s,n}$	0	0.5

Table II. Modeling parameters for a hybrid sodium-ion battery cathode half-cell with a polymer-ceramic hybrid electrolyte at room temperature.

Parameter	Value	References
Symmetry factors (α_a, α_c)	0.5	a)
NVP particle diameter (d_{NVP})	8 μm	a)
NaSICON particle diameter (d_{NAS})	4 μm	a)
Separator thickness (L_{sep})	20 μm	a)
Sodium max concentration ($c_{s,\text{max}}$)	14.2 mol l ⁻¹	b)
Sodium min concentration ($c_{s,\text{min}}$)	0 mol l ⁻¹	b)
Butler–Volmer reaction rate constant k	$3 \times 10^{-12} \text{ m}^{2.5} \text{ mol}^{0.5} \text{ s}^{-1}$	36
NVP/C conductivity (σ)	7.14 S cm ⁻¹	37
NaSICON conductivity (κ_{NAS})	$1.5 \times 10^{-3} \text{ S cm}^{-1}$	38
Polymer conductivity (κ_{pol})	$6 \times 10^{-5} \text{ S cm}^{-1}$	39
PEO–NaTFSI conductivity prefactor (K_{NaTFSI})	M ⁻¹	40
Peak polymer conductivity concentration ($c_{\text{el},\kappa_{\text{max}}}$)	$1.085 \times 10^{-3} \text{ S cm}^{-1}$	40
NaSICON diffusion coefficient ($D_{\text{el},\text{NAS}}$)	$4 \times 10^{-12} \text{ m}^2 \text{ s}^{-1}$	41
Polymer diffusion coefficient ($D_{\text{el},\text{pol}}$)	$4.7 \times 10^{-14} \text{ m}^2 \text{ s}^{-1}$	42
Sodium ion transference number (t_+^0)	0.39	39

a) geometric parameters used for simulation. b) calculated based on gravimetric capacity reported in Ref. 43.

Table III. Equilibrium potential model equations based on different equations of state.

Name	Equation	
1P Mar	$FU_{\text{eq}} = FU_{\text{eq}}^0 + RT \ln \left(\frac{1-\chi}{\chi} \right) + RT [-A(2\chi - 1)]$	[19]
2P Mar	$FU_{\text{eq}} = FU_{\text{eq}}^0 + RT \ln \left(\frac{1-\chi}{\chi} \right) + RT \left[-A + 2A\chi - B + 3B\chi - \frac{3}{2}B\chi^2 \right]$	[20]
van Laar	$FU_{\text{eq}} = FU_{\text{eq}}^0 + RT \ln \left(\frac{1-\chi}{\chi} \right) + RT \left[\frac{A(B\chi^2 - 1 + 2\chi - \chi^2)}{(1-\chi + B\chi)^2} \right]$	[21]
R-K	$FU_{\text{eq}} = FU_{\text{eq}}^0 + RT \ln \left(\frac{1-\chi}{\chi} \right) + \sum_{k=0}^N A_k \left[(2\chi - 1)^{k+1} - \frac{2k\chi(1-\chi)}{(2\chi - 1)^{1-k}} \right]$	[22]

cell, the subscript o denotes the own cell, and f denotes the value at the shared face, while Δ represents the face-to-cell distance with a correction for non-orthogonal cells.

Model parameterization.—The physics based model introduced a large set of parameters ideally directly measured or derived from measured quantities. The parameters with constant values used in the model are listed in Table II. However, the equilibrium potential determines the shape of the obtained polarization curves and is characteristic of the active material employed. Nevertheless, the sodium ion intercalation process lacks a robust theoretical description. The equilibrium potential of the Na⁺ intercalation electrodes deviates from the Nernst equation due to solid-state redox reactions, resulting in a distinctive anomalous voltage behavior, a topic extensively explored and debated in the literature.²⁵ Given the limited comprehension of solid-state redox reactions, experimental equilibrium potential profiles are typically matched to empirical expressions for subsequent model predictions.³¹ Karthikeyan et al. propose modeling the equilibrium potential of insertion electrodes using excess functions based on the principles of thermodynamics of non-ideal solutions.³² This approach expresses the equilibrium potential as a function of the mole fraction (χ) of the intercalating species and thermodynamic parameters. We compare thermodynamic equations such as one-parameter Margules (1P Mar), two-parameter Margules (2P Mar), van Laar and Redlich-Kister (R-K) equations to identify the most suitable thermodynamic equation.^{33,34} Table III provides a summary of the model equations used in this study.

Figure 3 shows the cell voltage measurements of carbon-coated NVP samples at low C-rates extracted from Si et al. and the corresponding fits to the thermodynamic equations.³⁵ A non-linear

least square algorithm was used for fitting the data to the equations. The fits were then assessed for both monotonicity and overall quality. Table IV presents the fit parameters for quality assessments. While the Redlich-Kister and one parameter Margules models exhibit high fit quality, they fail to adequately capture the elongated flat plateau and display non-monotonic behavior, which is physically unrealistic. In contrast, the two parameter Margules model, although

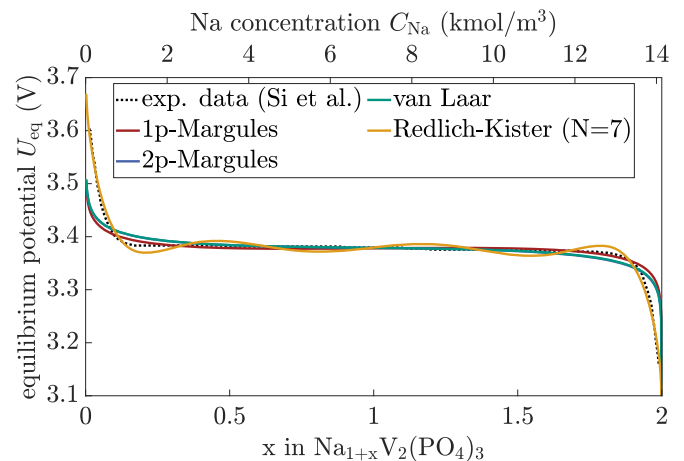


Figure 3. Cell voltage measurements of carbon-coated NVP samples at low C-rates, extracted from Si et al.³⁵ along with corresponding fits to thermodynamic equations. The fits were obtained using a non-linear least square algorithm.

Table IV. Fit parameters and quality assessments for the thermodynamic models.

Parameter	U_{eq}^0	A	B	R^2
1P Mar	0.3781	2.1698	0	0.9616
2P Mar	3.3782	1.5837	0.2306	0.9509
Van Laar	3.3785	1.81	1.0424	0.9507
Redlich-Kister	3.3787	^{a)}	0	0.9860

a) Coefficients are listed in Table A-I.

it may have a slightly lower fit quality, is preferred due to its ability to maintain monotonicity and its simpler formulation, making it more straightforward to interpret and apply in subsequent analyses.

Computational solution.—During discharge, Eqs. 5 through 7 describe the movement of Na coming from the anode, through the

electrolyte as Na^+ , and subsequently intercalating in the cathode active material. Simultaneously, charge conservation within the cathode, as well as ionic conservation within the electrolyte, are addressed through electric and ionic potentials. In the three-dimensional model, the sodium mass is represented by a single scalar, representing Na^+ within the electrolyte and Na within the electrode. Similarly, a second scalar is employed to depict potentials in the electrolyte and cathode phases. Numerically, these two scalars undergo discretization using unstructured tetrahedral cells with a second-order finite-volume spatial scheme and an implicit first-order temporal scheme. The equations are solved in a segregated manner, employing a conjugated gradient linear solver together with a geometric-algebraic multigrid solver for preconditioning the matrices. Each scalar is implicitly solved over the entire cathode and electrolyte domain. Solving uncoupled linear diffusion equations (e.g. Eq. 5) is straightforward and efficient, even on large, intricate, three-dimensional mesh networks. However, the significant non-linearity introduced by the electrochemistry (e.g. 13 and 12) and ion transport (e.g. migration terms in 8) complicate the computational solution considerably.

In the segregated solver, partial differential equations are solved for each computational domain individually. Figure 4 provides an overview of the iterative solution algorithm. Within the cathode domain, a sufficient number of inner and outer iterations are required to ensure consistency of the external current (I_s^{ex}), the current at the cathode–electrolyte interface (I_s^{cte}), and the current at the cathode current collector (I_s^{cc}) during galvanostatic cycling. The iterative coupling between the electrolyte and cathode domains is achieved through the Butler–Volmer charge transfer. To maintain computational stability, under-relaxation is applied when coupling the two computational domains. Convergence is evaluated by computing the normalized root mean square deviation (NRSMD) of respective currents on the coupled patches, $i_{\text{el}}^{\text{cte}}$ and i_s^{cte} , which must fall below the convergence criterion to ensure current consistency. Additionally, the change in concentration between successive iterations must be minimal. In the majority of simulation cases, convergence criteria δ_i of 1×10^{-3} were found to be sufficient.

Results and Discussion

This Section presents the impacts of polymer-ceramic cathode electrode characteristics on the battery performance, as predicted by the model. Through computational simulations, we explore how various properties of the cathode electrode, such as composition, microstructure, and thickness, may influence the overall performance metrics of the battery system. By analyzing these predictions, we seek insight into the underlying mechanisms that govern battery behavior, with the aim of informing future design strategies for enhanced battery performance.

Microstructure generation.—The cathode microstructures examined herein comprise a randomly arranged stack of dense, smooth, spherical particles, which were simulated using the discrete element method (DEM) via the open-source code LIGGGHTS. This approach is adapted from a LIB microstructure generation algorithm described in Ref. 44. The simulations aim to mimic the spatial distribution of the cathode components, without detailed modeling of particle interactions. The stack of particles, representing the active material and NaSICON fillers components, was generated within a simulation box and allowed to drop and roll under periodic boundaries, with collisions modeled using the Hertz-Mindlin model. This approach qualitatively replicates impedance measurement data.⁴⁵ The dimensions of the simulation box were set based on structural property studies. Uniaxial compression was applied to fix the cathode dimension, adjusting volume fractions. Electrodes were modeled at specific thicknesses for different studies. The particle stacks were extended and trimmed along the simulation box dimensions to ensure periodic cathode geometries and half-cells were formed. Pore volume within the cathode and a separator

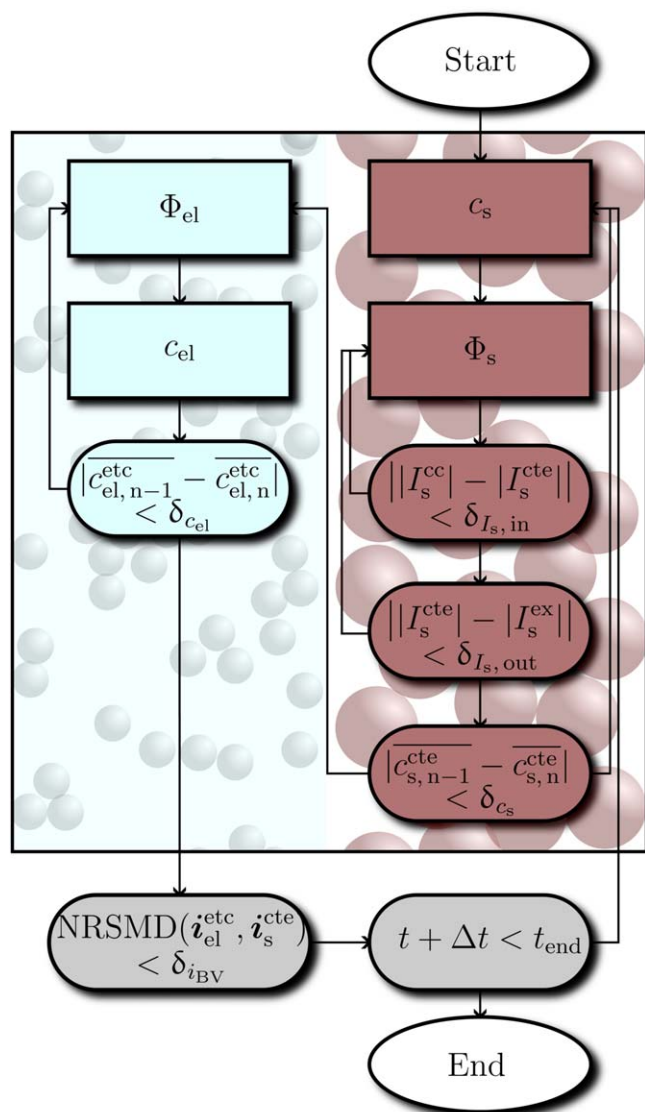


Figure 4. Schematic flowchart of the iterative solution algorithm used in the segregated solver. The algorithm ensures current consistency during galvanostatic cycling. Under-relaxation techniques are used to maintain stability, and the convergence of currents between the electrode and the electrolyte on the coupled patches is assessed using the normalized root mean square deviation (NRSMD) to confirm convergence.

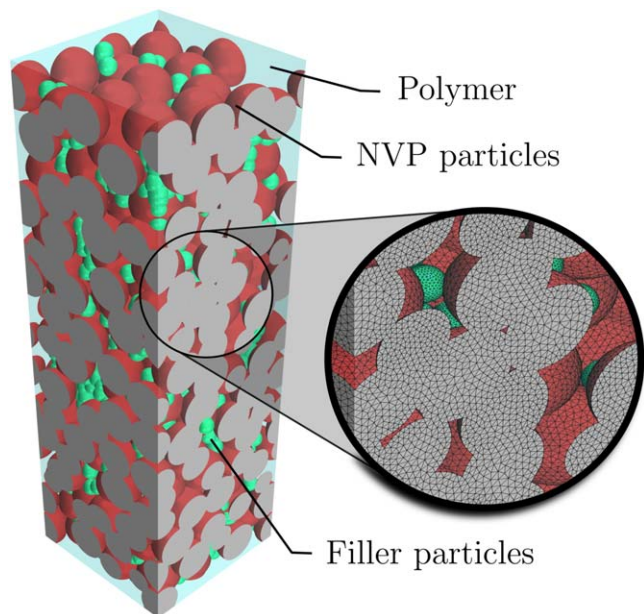


Figure 5. Schematic representation of the computational mesh and the cathode microstructure generated using the discrete element method (DEM) with LIGGGHTS software, showcasing the randomly arranged stack of dense, smooth, spherical particles. The simulation replicates the spatial distribution of the cathode components under periodic boundaries.

thickness were included to form the electrolyte domain. Pseudo-random number generation regulated the initial particle insertion. Multiple microstructures with different seeds were produced for each study, maintaining constant volume fractions and porosity for comparability. Figure 5 depicts a virtual cathode structure resulting from the described microstructure generation workflow. Finally, meshing of computational regions was performed using Simcenter. An example of the resultant unstructured tetrahedral mesh is illustrated in Fig. 5. The mesh generated by Simcenter maintains non-orthogonality within 65. To ensure accurate flux approximation and mitigate any potential issues arising from this non-orthogonality, corrections were applied to the surface normal gradient schemes and the Laplacian schemes in OpenFOAM®. These adjustments help maintain the accuracy of the spatial discretization used in the second-order finite volume method.

Filler content.—Figure 6 illustrates the discharging process for the battery system under investigation, wherein the active filler content in the electrolyte is varied. The NVP content was maintained at 54% with a cathode length of $100\ \mu\text{m}$. Such an electrode boasts a theoretical specific capacity of $204\ \text{mA h L}^{-1}$. In the course of the subsequent investigations, the electrolyte active filler volume fraction ($\varphi_{\text{el,fil}}$) was varied from 0% to 100%. The results demonstrate a large variation in utilized capacity varying from $21\ \text{mA h L}^{-1}$ for a pure PEO electrolyte to $202\ \text{mA h L}^{-1}$ for a pure NaSICON electrolyte. The premature termination of discharging in NaSICON-poor electrolytes is attributed to slow sodium ion transport within the electrolyte. Under galvanostatic cycling conditions, the net ionic current is dictated by the external current, resulting in a substantial potential difference within the electrolyte to enforce sodium ion transport, thus satisfying the charge transfer reaction demand. In particular, the electrode featuring an electrolyte active filler volume fraction of 80% falls short of utilizing the maximum capacity, exhibiting a slightly lower cell voltage compared to the electrode with a pure NaSICON electrolyte. However, this configuration assumes a denser packing than a close-packing of equal spheres without overlapping. To achieve such a high electrolyte active filler volume fraction in a real battery, the filler particles must deviate significantly from a spherical shape, given the need for electrolyte to

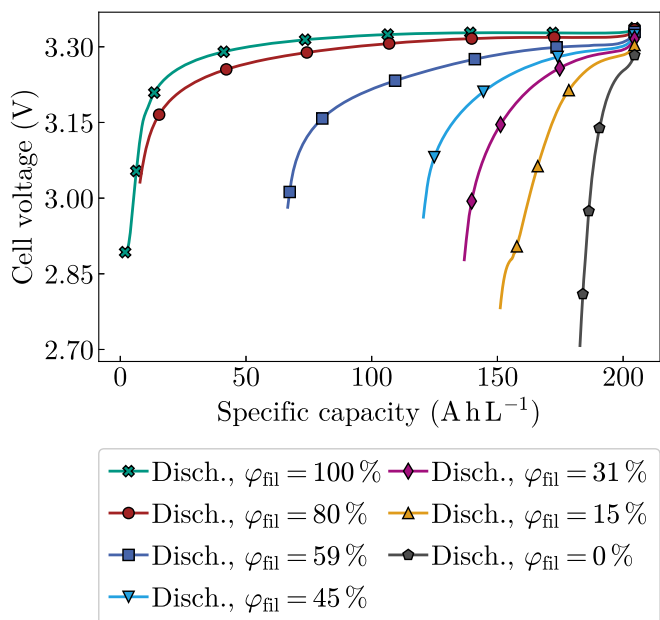


Figure 6. The solid lines represent the cell polarization curves of a sodium-ion battery with a hybrid composite solid electrolyte and varying electrolyte active filler volume fractions ($\varphi_{\text{el,fil}}$) at a cathode length of $100\ \mu\text{m}$ during C/5 discharging as a function of the specific capacity. Different colors and markers represent different electrolyte active filler volume fractions.

fill the void spaces between the active material particles. A configuration with an electrolyte active filler volume fraction of 59%, which is feasible with close-to-spherical filler particles without strong compression, utilizes $138\ \text{mA h L}^{-1}$ corresponding to 67% utilization of the theoretical capacity. Figure 7 depicts a C/5 charging process for the same electrolyte active filler volume fraction variants. As with the discharging process, nearly the entire theoretical capacity is utilized for a pure NaSICON electrolyte, with utilization decreasing with NaSICON content. During charging, this pattern is more evident, as the electrode with an 80% electrolyte

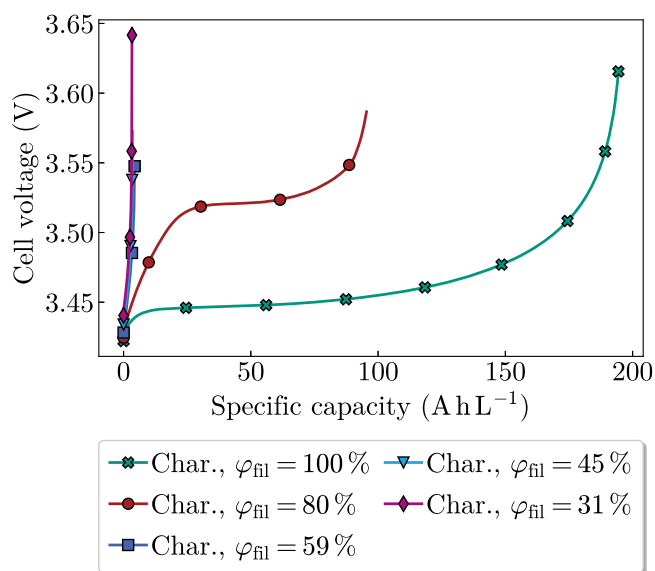


Figure 7. The solid lines represent the cell polarization curves of a sodium-ion battery with a hybrid composite solid electrolyte and varying electrolyte active filler volume fractions ($\varphi_{\text{el,fil}}$) at a cathode length of $100\ \mu\text{m}$ during C/5 charging as a function of the specific capacity. Different colors and markers represent different electrolyte active filler volume fractions.

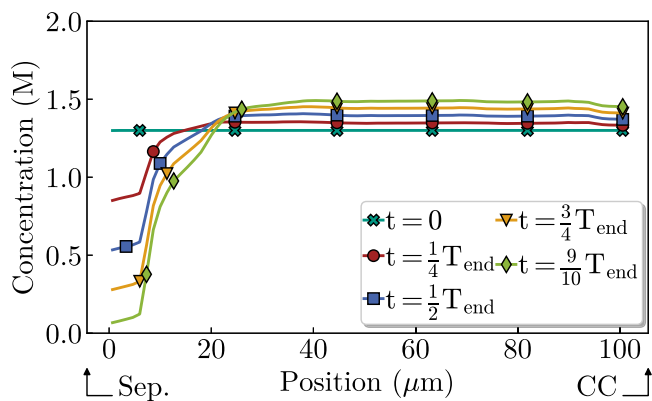


Figure 8. The solid lines represent the electrolyte sodium ion concentration (c_{el}) during C/5 charging. The electrolyte sodium ion concentration are averaged for positions between the separator (Sep.) and cathode current collector (CC).

active filler volume fraction achieves less than 50% of the theoretical capacity, whereas electrodes with reduced NaSICON content almost do not utilize any capacity. The simulations did not converge for electrolyte active filler volume fractions of less than 31%.

Examining the concentration distribution in the electrolyte elucidates the discrepancy in behavior between discharging and charging. Figure 8 presents the electrolyte sodium ion concentration averaged along the axis between the separator and the cathode current collector from the beginning of the charging process ($t = 0$) to close to the early termination of the charging process ($t = \frac{9}{10} T_{end}$). During the charging process, the sodium ion concentration near the separator undergoes a sharp decline from its initial concentration of 1.3 M to a concentration of nearly 0 M. This decline is a result of as sodium ions leaving the cathode half-cell at the separator enter the anode. Similar to the discharging process, the majority of the charge transfer reaction occurs in the area close to the separator. In the case of charging, the charge transfer reaction generates sodium ions in the electrolyte, which subsequently leave the half-cell at the separator. To counteract this sodium ion loss in the electrolyte near the separator, the formation of Na^+ deintercalating from the active material according to the Butler-Volmer reaction alone is insufficient. Hence, sodium ions must travel from the current collector to the separator which is hindered by slow Na^+ transport across the electrolyte. Additionally, according to Eq. 9 the conductivity of the polymer exhibits a pronounced decline for low electrolyte concentrations, resulting to a self-reinforcing phenomenon once the electrolyte concentration falls below a certain threshold.

Cathode thickness.—A thick cathode provides multiple benefits in a bipolar configuration. It decreases the number of necessary separators and current collectors, thereby reducing dead space and overall expenses. Figure 9 illustrates the simulated cell voltage over capacity per unit current collector area for cathode half-cells ranging from 70 μm to 250 μm in length. Throughout the simulations, the active material content ($55\% \pm 3\%$) and the electrolyte active filler volume fraction ($56\% \pm 3\%$) were maintained at consistent levels within the margins of error associated with microstructure generation and meshing. The initial discharge rate was set to 0.2 C. As anticipated, thicker cathodes achieve higher capacities, with the thickest cathode (250 μm) reaching approximately 2 mA h cm^{-2} compared to the thinnest electrode (70 μm) with a capacity of 0.8 mA h cm^{-2} . It is notable that as the thickness of the cathode half-cell increases from the thinnest to the thickest, the depth of discharge declines from 60% to 40%. This decline implies that a considerable proportion of the theoretical capacity cannot be effectively utilized for thicker cathodes.

Active material content.—Figure 10 presents the cell voltages plotted against the specific capacity for cathode electrodes featuring

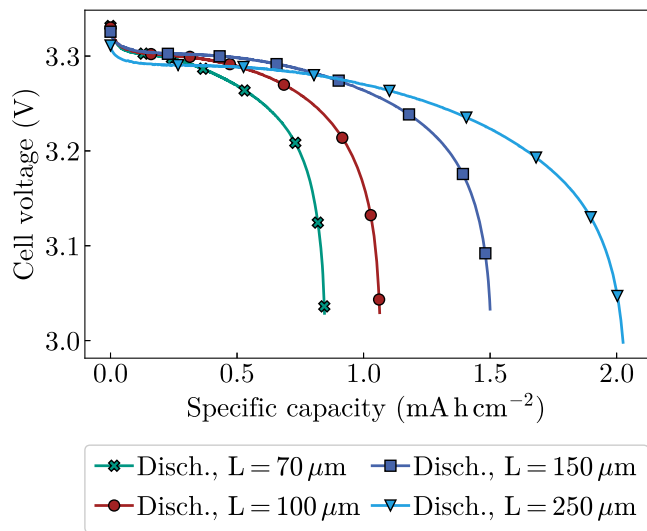


Figure 9. The solid lines represent the cell polarization curves of a sodium-ion battery with a hybrid composite solid electrolyte, an active material content of ($55 \pm 3\%$) and an electrolyte active filler volume fraction of ($56 \pm 3\%$) with varying cathode length.

different NVP contents. The electrolyte active filler volume fraction was kept constant at 50% with a cathode length of 100 μm . Discharging takes place under galvanostatic conditions at a C-rate of 0.2. Discharging was terminated significantly earlier for the cathodes with lower porosity. For instance, the cathode containing 80% NVP content reaches an SOC of 0.9, whereas the cathode with 39% NVP content terminates discharging below an SOC of 0.1. Upon closer examination, this discrepancy is attributed to Na^+ transport in the electrolyte. In Fig. 11, a cross-section of the cathode electrode, spanning from the separator to the current collector, is depicted. Two distinct color maps illustrate the sodium ion

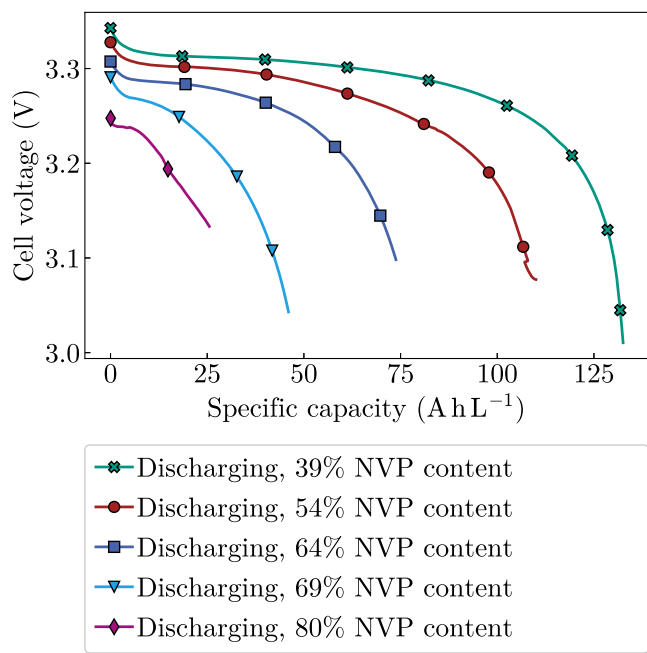


Figure 10. The solid lines represent the cell polarization curves of a sodium-ion battery with a hybrid composite solid electrolyte, a cathode length of 100 μm and an electrolyte active filler volume fraction of 50% under C/5 discharging as a function of the specific capacity. Different colors and markers represent different active material contents.

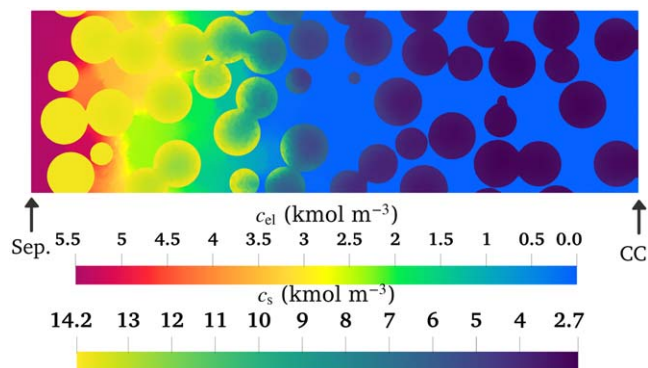


Figure 11. Cross Section of a sodium-ion battery cathode with a hybrid composite solid electrolyte between the separator (left) and the current collector (right). The colors indicate the active material sodium concentration (c_s) and electrolyte sodium ion concentration (c_{el}).

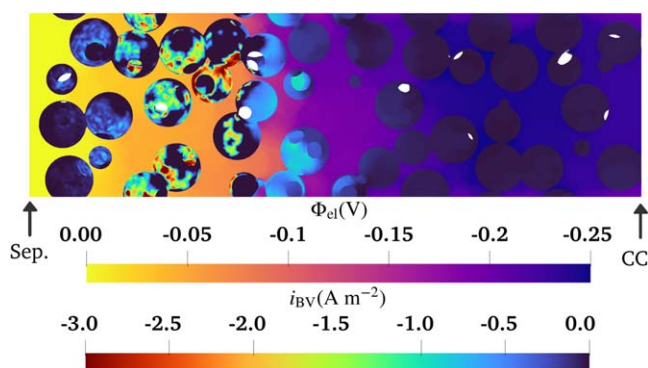


Figure 12. Cross Section of a sodium-ion battery cathode with a hybrid composite solid electrolyte between the separator (left) and the current collector (right). The colors indicate the ButlerVolmer current density (i_{BV}) at the cathode–electrolyte interface and the electrolyte potential (Φ_{el}).

concentration in both the electrolyte and the active material. The electrolyte ionic conductivity is lower than the electronic conductivity of the cathode. Consequently, current flow minimizes the time spent in the electrolyte, leading to the charge transfer reaction primarily occurring near the separator. During the discharging process, the charge transfer reaction gradually shifts from the separator region toward the current collector as the active material particles adjacent to the separator reach the maximum sodium concentration. This necessitates an increase in electrolyte potential to facilitate ionic current penetration deeper into the positive half-cell. This dependency is non-linear, resulting in a significant drop in electrolyte potential, consequently lowering the cell potential eventually. Figure 12 provides insight into the electrolyte potential and the ButlerVolmer current density at the cathode–electrolyte interface toward the end of the discharge process. Following convention, the ButlerVolmer current density has a negative sign during discharging. Notably, regions with a high magnitude of ButlerVolmer current density move away from the separator, where the exchange current density diminishes due to the active material sodium ion concentration nearing its maximum limit of 14.2 M. To drive the ionic current deeper into the electrode, the electrolyte potential drop exceeds 250 mV.

Conclusions

The cell design and cell composition can negatively impact the utilization and therewith resource efficiency of all-solid-state sodium-ion batteries and limit the performance of the batteries. Although the integration of ultrahigh contents of fast-ion-transporting inorganic ceramics in the electrolyte may seem intuitive, practical limitations in

real-world applications must be considered. To gain deeper insight into the underlying processes affecting macroscopic quantities such as cell voltage and state of charge, we developed and parameterized a physical model that allows simulations at the particle scale. Our microstructure generation approach involved creating cathode microstructures composed of dense, smooth, spherical particles using the discrete element method, with the goal of replicating real cathodes. We identified slow Na^+ transport throughout the electrolyte as a major bottleneck for cell performance. This sluggish Na^+ transport is mainly attributed to three factors: the low porosity of the half-cell due to the high active material content, the substantial distance between the separator and the current collector resulting from the large half-cell thickness, and the overall low electrolyte ionic conductivity due to the low active filler content. These factors lead to high Na^+ gradients in the electrolyte, particularly near the separator, for moderate C-rates. Our simulations indicate that at room temperature, electrodes with an electrolyte active filler volume fraction of 80% and electrode thicknesses of 100 μm and smaller are required to achieve sufficient utilization of the theoretical battery capacity. These results emphasize the importance of further advancing fast-ion conducting solid electrolytes in the development of all-solid-state sodium-ion batteries. During charging, Na^+ are predominantly consumed near the separator severely limiting utilization except for very high electrolyte active filler volume fractions. While further investigation is warranted, these insights provide valuable guidance for the ongoing technical advancement of cathode half-cells for sodium-ion batteries with hybrid polymer-ceramic electrolytes. These findings highlight the intricate relationship between electrode microstructure and battery performance, offering valuable insights for the design and optimization of sodium-ion battery systems.

Together with sodium metal anodes, the battery system shows potential for sustainable batteries for stationary applications or mobile applications with less stringent energy density constraints.

Acknowledgments

The authors acknowledge funding and support from the German Federal Ministry of Education and Research (Bundesministerium für Bildung und Forschung) under project number 03XP0403D. The responsibility for the content is with the authors. Additionally, this research received support from the state of Baden-Württemberg through bwHPC. We also appreciate the use of OpenAI's ChatGPT, based on the GPT-3.5 architecture, for its assistance in the grammar and language review of this manuscript. The AI was used to improve clarity and readability, but it did not contribute to the scientific or experimental content of the work.

Appendix

Appendix A.1. Derivation and fitting of the electrolyte conductivity equation.—Mongcopa et al. used quasi-elastic neutron scattering (QENS) to study the conductivity of PEO at different Li^+/EO ratios (r_s) and derived the following dependence of conductivity on LiTFSI salt concentration:²⁹

$$\sigma = 0.043r_s \left[\exp\left(-\frac{r_s}{0.085}\right) \right] \quad [\text{A} \cdot 1]$$

They attributed the constants 0.043 and 0.085 to the specific conductivity of the dilute electrolyte and the exponential slowing of segmental relaxation in the presence of salt, respectively. To align with the formulation of the physics-based model, we express the equation in terms of c_{el} rather than r_s . Mathematically, the numerator in the exponent represents the abscissa at the maximum turning point of the function which corresponds to the concentration at the peak polymer conductivity ($c_{el, \kappa_{\text{max}}}$). In our reformulated equation, a single empirical constant remains, specific to the materials used and denoted as K_{NaTFSI} in this study (see Eq. 9). The data fit to evaluate the value, based on data from Ferry et al., is shown in Fig. A-1.⁴⁰

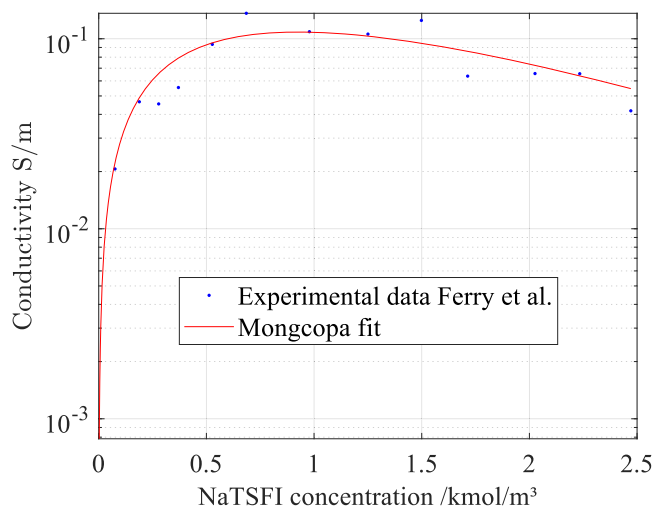


Figure A-1. Experimental values of electrolyte conductivity from Ferry et al.⁴⁰ compared to the fitted conductivity function derived in this study.

Appendix A.2. Fit parameters for the Redlich-Kistner Thermodynamic Model

Table A-I. Fit parameters and quality assessments for the Redlich-Kistner thermodynamic model.

U_0/V	3.3787
A_0	4242
A_1	-170.67
A_2	-6814.2
A_3	1406.3
A_4	302 201
A_5	-3549.3
A_6	-37732
A_7	3876.5

ORCID

F. Gerbig <https://orcid.org/0000-0003-3059-0171>

A. Chauhan <https://orcid.org/0000-0002-4871-178X>

References

- T. Jin, H. Li, K. Zhu, P. F. Wang, P. Liu, and L. Jiao, *Chem. Soc. Rev.*, **49**, 2342 (2020).
- C. Delmas, *Adv. Energy Mater.*, **8**, 1703137 (2018).
- P. K. Nayak, L. Yang, W. Brehm, and P. Adelhelm, *Angewandte Chemie (International ed. in English)*, **57**, 102 (2018).
- M. M. Titirici, *Sodium-Ion Batteries* (Wiley-VCH, Weinheim) (2022).
- Y. Liu, J. Li, Q. Shen, J. Zhang, P. He, X. Qu, and Y. Liu, *eScience*, **2**, 10 (2022).
- R. Usiskin, Y. Lu, J. Popovic, M. Law, P. Balaya, Y. S. Hu, and J. Maier, *Nature Reviews Materials*, **6**, 1020 (2021).
- C. Li, H. Xu, L. Ni, B. Qin, Y. Ma, H. Jiang, G. Xu, J. Zhao, and G. Cui, *Adv. Energy Mater.*, **13**, 2301758 (2023).
- L. Fan and X. Li, *Nano Energy*, **53**, 630 (2018).
- Q. Liu, X. Zhao, Q. Yang, L. Hou, D. Mu, G. Tan, L. Li, R. Chen, and F. Wu, *Advanced Materials Technologies*, **8**, 2200822 (2023).
- G. G. Eshetu, G. A. Elia, M. Armand, M. Forsyth, S. Komaba, T. Rojo, and S. Passerini, *Adv. Energy Mater.*, **10**, 2000093 (2020).
- Y. Dong, P. Wen, H. Shi, Y. Yu, and Z. S. Wu, *Advanced Functional Materials*, **34**, 2213584 (2023).
- Z. Zou et al., *Chem. Rev.*, **120**, 4169 (2020).
- Z. Zhang, Q. Zhang, C. Ren, F. Luo, Q. Ma, Y. S. Hu, Z. Zhou, H. Li, X. Huang, and L. Chen, *Journal of Materials Chemistry A*, **4**, 15823 (2016).
- M. Chen et al., *Nat. Commun.*, **10**, 1480 (2019).
- G. Ávall, J. Mindemark, D. Brandell, and P. Johansson, *Adv. Energy Mater.*, **8**, 1703036 (2018).
- E. J. Kim, P. R. Kumar, Z. T. Gossage, K. Kubota, T. Hosaka, R. Tatara, and S. Komaba, *Chemical Science*, **13**, 6121 (2022).
- H. Xiang, Y. Wang, K. Li, X. Zhang, and Z. Chen, *Journal of Energy Storage*, **72**, 108314 (2023).
- K. Chayambuka, G. Mulder, D. L. Danilov, and P. H. Notten, *Electrochimica Acta*, **404**, 139764 (2022).
- V. K. Garapati, N. N. Dingari, M. Mynam, and B. Rai, *J. Electrochem. Soc.*, **170**, 010517 (2023).
- H. Darjazi, M. Falco, F. Colò, L. Balducci, G. Piana, F. Bella, G. Meligrana, F. Nobili, G. A. Elia, and C. Gerbaldi, *Advanced materials (Deerfield Beach, Fla.)*, e2313572 (2024).
- S. Cernak, F. Gerbig, M. Kespe, and H. Nirschl, *Energy Storage*, **2**, e156 (2020).
- G. M. Goldin, A. M. Colclasure, A. H. Wiedemann, and R. J. Kee, *Electrochimica Acta*, **64**, 118 (2012).
- M. Kespe and H. Nirschl, *International Journal of Energy Research*, **39**, 2062 (2015).
- J. Newman and N. P. Balsara, *Electrochemical Systems, The Electrochemical Society Series* (Wiley, Hoboken, NJ) 4th edn ed. (2021) 978-1-119-51460-2.
- G. Chen, Q. Huang, T. Wu, and L. Lu, *Adv. Funct. Mater.*, **30**, 2001289 (2020).
- S. A. Novikova, R. V. Larkovich, A. A. Chekannikov, T. L. Kulova, A. M. Skundin, and A. B. Yaroslavtsev, *Inorganic Materials*, **54**, 794 (2018).
- G. L. Plett, *Battery management systems: Vol 1: battery modeling* (Artech House, Boston and London) Artech House Power Engineering and Power Electronics, (2015) 978-1-63081-023-8.
- K. E. Thomas, J. Newman, and R. M. Darling, "Mathematical modeling of lithium batteries," *Advances in Lithium-Ion Batteries*, ed. W. A. van Schalkwijk and B. Scorsati (Kluwer Academic/Plenum Publ, New York) p. 345 (2002).
- K. I. S. Mongcopa, M. Tyagi, J. P. Mailoa, G. Samsonidze, B. Kozinsky, S. A. Mullin, D. A. Gribble, H. Watanabe, and N. P. Balsara, *ACS Macro Letters*, **7**, 504 (2018).
- M. Z. Bazant, *Faraday Discussions*, **246**, 60 (2023).
- C. Sequeira and A. Hooper, *Solid State Ionics*, **9-10**, 1131 (1983).
- D. K. Karthikeyan, G. Sikha, and R. E. White, *Journal of Power Sources*, **185**, 1398 (2008).
- O. Redlich and A. T. Kister, *Industrial & Engineering Chemistry*, **40**, 341 (1948).
- S. M. Walas, *Phase Equilibria in Chemical Engineering* (Butterworth Publishers, Stoneham, Massachusetts) (1985).
- L. Si, Z. Yuan, L. Hu, Y. Zhu, and Y. Qian, *Journal of Power Sources*, **272**, 880 (2014).
- H. Gao, L. Xue, S. Xin, K. Park, and J. B. Goodenough, *Angewandte Chemie (International ed. in English)*, **56**, 5541 (2017).
- X. Liu, G. Feng, E. Wang, H. Chen, Z. Wu, W. Xiang, Y. Zhong, Y. Chen, X. Guo, and B. Zhong, *ACS Applied Materials & Interfaces*, **11**, 12421 (2019).
- M. Kaus, M. Guin, M. Yavuz, M. Knapp, F. Tietz, O. Guillon, H. Ehrenberg, and S. Indris, *The Journal of Physical Chemistry C*, **121**, 1449 (2017).
- J. Serra Moreno, M. Armand, M. B. Berman, S. G. Greenbaum, B. Scorsati, and S. Panero, *Journal of Power Sources*, **248**, 695 (2014).
- A. Ferry, M. M. Doeff, and L. C. de Jonghe, *J. Electrochem. Soc.*, **145**, 1586 (1998).
- F. Moradipour, A. Markert, T. Rudsuck, N. Röttgen, G. Dück, M. Finsterbusch, F. Gerbig, H. Nirschl, and G. Guthausen, *Journal of Energy and Power Technology*, **05**, 1 (2023).
- P. Wróbel, P. Kubisiak, and A. Eilmes, *The Journal of Physical Chemistry B*, **125**, 10293 (2021).
- Q. Zheng, H. Yi, W. Liu, X. Li, and H. Zhang, *Electrochimica Acta*, **238**, 288 (2017).
- A. Chauhan, E. Asylbekov, S. Kespe, and H. Nirschl, *Electrochemical Science Advances*, **3**, e2100151 (2023).
- S. Hein et al., *J. Electrochem. Soc.*, **167**, 013546 (2020).